Version: 26.02.2022

Water-based synthesis of ultrasmall nanoparticles of platinum group metal oxides (1.8 nm)

Oliver Wetzel,[1] Oleg Prymak,[1] Kateryna Loza,[1] Nina Gumbiowski,[1] Marc Heggen,[2] Peter Bayer,[3] Christine Beuck,[3] Claudia Weidenthaler,[4] and Matthias Epple[1]*

[1] Inorganic Chemistry and Center for Nanointegration Duisburg-Essen (CeNIDE), University of Duisburg-Essen, Universitaetsstr. 5-7, 45117 Essen, Germany

[2] Ernst Ruska-Centre for Microscopy and Spectroscopy with Electrons, Forschungszentrum Jülich GmbH, 52425 Jülich, Germany

[3] Department of Structural and Medicinal Biochemistry, Centre for Medical Biotechnology (ZMB), University of Duisburg-Essen, Universitaetsstr. 5-7, 45117 Essen, Germany

[4] Max-Planck-Institut für Kohlenforschung, Kaiser-Wilhelm-Platz 1, 45470 Mülheim an der Ruhr, Germany

* Corresponding author. e-mail: matthias.epple@uni-due.de

Abstract

Ultrasmall nanoparticles of platinum group metal oxides (core diameter about 1.8 nm) were prepared by alkaline hydrolysis of metal precursors in the presence of $NaBH_4$ and by colloidal stabilization with the tripeptide glutathione. We obtained water-dispersed nanoparticles of Rh_2O_3, PdO, RuO_2, IrO_2, Os/OsO_2, and Pt/PtO. Their size was probed by high-resolution transmission electron microscopy, disc

centrifugal sedimentation, small-angle X-ray scattering (SAXS), and diffusion-ordered ^{1}H-NMR spectroscopy (^{1}H-DOSY). Their oxidation state was clearly determined by X-ray photoelectron spectroscopy (XPS), X-ray powder diffraction (XRD), and electron diffraction. The chemical composition of the nanoparticles, i.e. the ratio of metal oxide core and glutathione capping agent, was quantitatively determined by a combination of these methods.

Keywords: Nanoparticles; NMR spectroscopy; glutathione; X-ray photoelectron spectroscopy; platinum group metals; metal oxides

Introduction

Nanoparticles of noble metal oxides are of high importance in materials science, e.g. in heterogeneous catalysis or electrocatalysis. Their reactivity occurs mainly on their surface, therefore it is important to create them with a small particle size ("ultrasmall") that in turn leads to a high specific surface area.[1-9] Furthermore, ultrasmall metallic nanoparticles, usually consisting of metallic gold,[10-14] have been proposed for biomedical applications, e.g. to target proteins or tissues.[15] With ultrasmall silver nanoparticles, a possible bactericidal effect of silver can be exploited.[16-19] In general, such small particles with a size below 2 nm are close to the size of metalloid clusters with atom-sharp composition.[20-25]

Here we report on a facile synthesis to create ultrasmall nanoparticles of platinum group metal oxides by wet-chemical synthesis. This was accomplished by alkaline hydrolysis induced by $NaBH_4$, followed by colloidal stabilization with the tripeptide glutathione (GSH) in a modified Brust-Schiffrin synthesis.[26, 27] Notably, an unequivocal identification of their chemical nature (oxides) was only possible by a combination of X-ray powder diffraction, X-ray photoelectron spectroscopy, and electron diffraction.

Experimental

Chemicals

For the synthesis of metal oxide nanoparticles, we used ruthenium(+III) chloride ($RuCl_3$, Sigma-Aldrich), rhodium(+III) chloride ($RhCl_3$, Sigma-Aldrich, p.a.), palladium(II) nitrate in 2 % HNO_3 ($Pd(NO_3)_2$, Bernd Kraft GmbH, p.a.), hexachloridoosmium(+IV) acid (H_2OsCl_6, Sigma-Aldrich, p.a.), sodium hexachloridoiridate (+IV) ($Na_2[IrCl_6]$, Sigma-Aldrich, p.a.) hexachloridoplatinum(+IV) acid (H_2PtCl_6, Sigma-Aldrich, p.a.), and sodium borohydride ($NaBH_4$, Fluka, 96%). The particles were coated with the tripeptide L-glutathione (GSH, Sigma Aldrich, 98%) during the synthesis for colloidal stabilization.

Ultrapure water with a specific resistivity of 18.2 MΩ was prepared with a Purelab ultra instrument (ELGA) and used for all experiments unless noted otherwise. All glassware was cleaned with boiling *aqua regia* and washed thoroughly with ultrapure water before use. In the following the glutathione-coated particles are denoted as M-GSH with M the different metals and metal oxides. All syntheses were performed under argon atmosphere (Schlenk technique).

Nanoparticle synthesis

For all syntheses, 7.5 mg $NaBH_4$ (200 µmol) was freshly dissolved in 1 mL cold water. It hydrolyses under formation of hydroxide and hydrogen and leads to a basic pH. The synthesis was started under acid conditions due to the acidic metal precursors. The pH then turned alkaline after $NaBH_4$ was added, leading to the hydrolytic formation of metal oxides. Basically, we have adapted a Brust-Schiffrin synthesis [26, 27] that is usually applied to generate ultrasmall gold and silver nanoparticles to platinum group metals.

For the synthesis of RuO_2-GSH nanoparticles, 4 mg glutathione (13 µmol) was dissolved in 13 mL degassed water. 2 mL (1 g L^{-1}; 19.8 µmol) ruthenium(+III)

chloride solution in 2% HCl was added, and the reaction mixture was refluxed for 1 h. The heat source was removed and the $NaBH_4$ solution was added under vigorous stirring. The mixture was stirred for one more hour until a black particle dispersion had formed.

For the synthesis of Rh_2O_3-GSH nanoparticles, 4 mg glutathione (13 µmol) was dissolved in 14 mL degassed water. 1 mL (2 g L^{-1}; 19.8 µmol) rhodium(+III) chloride solution was added, and the reaction mixture was stirred for 30 min at room temperature. The $NaBH_4$ solution was added under vigorous stirring. The mixture was stirred for 12 h until a black particle dispersion had formed.

For the synthesis of PdO-GSH nanoparticles, 7 mg glutathione (22.8 µmol) was dissolved in 10 mL degassed water. 10 mL (0.2 g L^{-1}; 17.9 µmol) palladium(+II) nitrate solution was added, and the reaction mixture was stirred for 30 min at room temperature. The $NaBH_4$ solution was added under vigorous stirring. The mixture was stirred for 1 h until a dark orange particle dispersion had formed.

For the synthesis of Os/OsO_2-GSH nanoparticles, 3 mg glutathione (9.8 µmol) was dissolved in 13 mL degassed water. 0.5 mL (4 g L^{-1}; 10.5 µmol) hexachloridoosmium(+IV) acid solution was added. The reaction mixture was refluxed for 1 h. The heat source was removed and the $NaBH_4$ solution was added under vigorous stirring. The mixture was stirred for one more hour until a black particle dispersion had formed.

For the synthesis of IrO_2-GSH nanoparticles, 10 mg glutathione (32.5 µmol) was dissolved in 12 mL degassed water. 2.8 mL (0.72 g L^{-1}; 10.4 µmol) sodium hexachloridoiridate(+IV) solution was added, and the reaction mixture heated to boiling. The $NaBH_4$ solution was added under vigorous stirring. The mixture was stirred for 2 h. The heat source was removed, and the yellow particle dispersion was cooled to room temperature.

For the synthesis of PtO-GSH nanoparticles, 1.5 mg glutathione (4.9 µmol) was dissolved in 12.5 mL degassed water. 2.5 mL (0.8 g L^{-1}; 10.3 µmol)

hexachloridoplatinum(+IV) acid solution was added. The reaction mixture was stirred for 1 h. The $NaBH_4$ solution was added under vigorous stirring. The mixture was stirred for 30 min until a dark-orange dispersion had formed.

After the synthesis, all particle dispersions were purified by multiple centrifugation through an ultra-filtration spin column (MWCO 3 kDa, 15 mL; Amicon; Merck) for 45 min at 4,000 rpm (2,500g), followed by washing with water.

Analytical methods

The concentrations of ruthenium, palladium, and platinum in the nanoparticle dispersions were determined by atomic absorption spectroscopy (AAS) with a Thermo Electron M-Series spectrometer (graphite tube furnace; procedure according to DIN EN ISO/IEC 17025:2005) after dissolving the nanoparticles in *aqua regia*. The concentrations of osmium, rhodium and iridium were determined by inductively coupled plasma mass spectrometry (ICP-MS) with a PE Nexion 2000 instrument (procedure according to DIN EN ISO 17294-2) at Indikator GmbH (Wuppertal, Germany).

Analytical disc centrifugation (differential centrifugal sedimentation; DCS) was performed with a CPS Instruments DC 24000 disc centrifuge (24,000 rpm). Two sucrose solutions (8 wt% and 24 wt%) formed a density gradient that was capped with 0.5 mL dodecane as stabilizing agent. The calibration standard was a poly(vinyl chloride) (PVC) latex in water with a particle size of 483 nm provided by CPS Instruments. A calibration was carried out prior to each run. A sample volume of 100 µL of dispersed nanoparticles was used. The measuring time was about 10 h at the given centrifugation speed due to the small particle size. The densities of ruthenium(+IV) oxide (6.97 g cm^{-3}), rhodium(+III) oxide (8.2 g cm^{-3}), palladium(+II) oxide (8.3 g cm^{-3}), osmium (22.59 g cm^{-3}), iridium(+IV) oxide

(11.66 g cm^{-3}), and platinum(+II) oxide (14.17 g cm^{-3}) were used for the computations.

UV-VIS spectroscopy was performed with a Varian Cary 300 instrument from 200 to 800 nm after background solvent correction (PBS buffer). Suprasil® quartz glass cuvettes with a sample volume of 500 µL were used.

High-resolution transmission electron microscopy was performed with an aberration-corrected FEI Titan transmission electron microscope equipped with a Cs-probe corrector (CEOS Company) operating at 300 kV.[28] Fast Fourier transformations of single particle images were performed and analyzed by the CrysTBox software.[29]

The HRTEM images were quantitatively analyzed by a custom-made machine learning-based approach implemented in Matlab. The program used a deeplab v3+ network for semantic segmentation which was trained on 2200 labelled HRTEM image slices of ultrasmall and standard nanoparticles. The network was trained using transfer learning and initialized with weights from a resnet18 network trained on natural images. It had an accuracy of 97% on the test dataset. For the extraction of particle properties such as Feret diameter, equivalence diameter and circularity, all particles connecting to the image boundary were excluded to avoid cutting effects.

For NMR spectroscopy, about 10 mg of the GSH-coated nanoparticles were dispersed in 500 µL D_2O (pH 8.3). 1D-NMR spectra (^1H, ^{13}C) and 2D-NMR spectra (^1H-^1H-COSY, ^1H-^{13}C-HSQC, ^1H-^{13}C-HMBC) were recorded with an Avance III 600 MHz spectrometer (Bruker, Rheinstetten, Germany) equipped with a Prodigy cryo probe head. Due to the low ligand concentration in the aqueous dispersions, all ^1H-NMR spectra were recorded with simultaneous suppression of the water signal by excitation sculpting; the excited spectral range had a width of approximately 0.6 ppm. The number of GSH molecules on the

particle surface was determined by quantitative ^{1}H-NMR spectroscopy with maleic acid as internal standard.

^{1}H-DOSY NMR spectroscopy was performed with a Bruker Avance III 700 MHz spectrometer with a 5 mm TCI ^{1}H/^{13}C/^{15}N/D cryoprobe with a *z*-gradient at 25 °C. The remaining water signal was suppressed by adding a pre-saturation pulse to the ^{1}H-DOSY pulse sequence from the Bruker library. The DOSY diffusion time Δ was 100 ms for all samples, with a pulsed gradient duration δ of 2 ms for free glutathione and 3.5 ms for GSH-coated nanoparticles. The gradient strength was incrementally increased in a linear fashion from 5 to 95% of the maximum gradient strength (50.4 G cm^{-1} for a smoothed square gradient pulse) in 32 steps for each pseudo-2D DOSY data set.

The spectra were Fourier-transformed, phased, and integrated with the program Topspin 3.5 (Bruker). The linearized diffusion data were plotted and fitted according to the Stejskal-Tanner equation[30, 31]

$$\ln\left(\frac{I}{I_0}\right) = -\gamma^2\delta^2\left(\Delta - \delta/3\right)\cdot D\cdot G^2 \qquad (1)$$

with I the signal intensity, I_0 the signal intensity without gradient, γ the gyromagnetic ratio of ^{1}H, δ the diffusion gradient pulse length, Δ the diffusion delay, G the gradient strength, and D the translational diffusion coefficient.

The Stejskal-Tanner plots of four well-discernible proton signals of free glutathione (3.7 ppm, 3.0 ppm, 2.55 ppm, 2.15 ppm) and three signals of GSH-coated nanoparticles (3.8 ppm, 2.5 ppm, 2.1 ppm) were first analyzed separately. Upon yielding the same diffusion coefficient within the error margin, the relative intensities I/I_0 of all signals were averaged. Error bars of the averaged data points represent the standard deviation. The given accuracy of the diffusion coefficient is the standard deviation of the Stejskal-Tanner fit.

The hydrodynamic diameter was calculated according to the Stokes-Einstein equation

$$d_H = \frac{k_B \cdot T}{3\pi \cdot \eta \cdot D} \quad (2)$$

with d_H the hydrodynamic diameter, k_B the Boltzmann constant, T the temperature in K, η the dynamic viscosity of D_2O at 25 °C,[32] and D the translational diffusion coefficient.

X-ray photoelectron spectroscopy (XPS) was performed with a spectrometer from SPECS GmbH equipped with a Phoibos 150 1D-DLD hemispherical energy analyzer. The monochromatized Al Kα X-ray source (E=1486.6 eV) was operated at 15 kV and 200 W. For high-resolution scans, the pass energy was set to 20 eV. The medium area mode was used as lens mode. The base pressure in the analysis chamber was $5 \cdot 10^{-10}$ mbar during the experiment. To account for charging effects, all spectra were referred to C 1s at 284.5 eV.

X-ray powder diffraction (XRD) was performed on a D8 Advance powder diffractometer (Bruker) in Bragg-Brentano reflection mode with Cu Kα radiation (λ=1.54 Å; U=40 kV, I=40 mA, line focus). A dispersion of GSH-coated nanoparticles was mixed with microcrystalline LaB_6 standard powder from NIST (SRM 660b) and placed on a silicon single crystal sample holder to minimize scattering. After drying in air, each sample was measured from 20 to 90° 2Θ with a step size of 0.02° and a counting time of 20 s, resulting in a total measurement time of 13.6 h. Qualitative phase analysis was performed with Diffrac.Suite EVA V1.2 from Bruker with the patterns of the metals Ru (#06-0663), Rh (#05-0685), Pd (#46-1043), Os (#06-0662), Ir (#46-1044), Pt (#04-0802), and the oxides RuO_2 (#87-0726), Rh_2O_3 (#41-0541), PdO (#41-1107), OsO_2 (#43-1044), IrO_2 (#15-0870), PtO (#47-1171) as well as LaB_6 (#34-0427) from the ICDD database. Quantitative Rietveld refinement was performed with the Bruker software

TOPAS 5.0 to calculate the lattice parameters and the average crystallite size *CS* from diffraction peak broadening[33]

$$CS = \frac{\mathrm{K}\cdot\lambda}{IB\cdot\cos\theta} \tag{3}$$

with K a constant set to 0.89 (assuming a spherical particle shape), λ the wavelength of the X-radiation, *IB* the integral breadth of the diffraction peaks in radians (after considering the instrumental peak broadening), and Θ the diffraction angle. The reference material LaB_6 was necessary for instrumental parameter correction and the precise determination of the sample displacement as refined in the Rietveld procedure.

Small-angle X-ray scattering (SAXS) was performed on an Empyrean diffractometer (Panalytical) in transmission mode with an evacuated beam path chamber ScatterX-78 (vacuum $5\cdot10^{-2}$ mbar), Cu Kα radiation (λ=1.54 Å, *U*=40 kV and *I*=40 mA, line focus), and a sample-to-detector distance of 240 mm (PIXcel^{3D} detector). For the measurements, a glass capillary from Hilgenberg GmbH (length 80 mm, outer diameter 1 mm, wall thickness 0.01 mm) was filled with a colloidal dispersion of GSH-coated nanoparticles in water. For background correction, the same capillary was filled with water and measured again. All samples were measured in the 2Θ range of −0.15° to +5.00° at a step size 0.01° with a total measurement time of 21 min. For the SAXS data processing, a polydisperse system of spheres was assumed and analyzed with the indirect Fourier transformation (IFT) program GNOM[34] implemented in the EasySAXS software 2.0 from Panalytical. From the measured scattering intensity, $I(q)$, the volume-weighed size distribution (D_V) was determined (eq. 4) after the form factor for the spheres (P_{sph}) was computed (eq. 5). The following equations were used:

$$I(q) = c_v \int_0^\infty D_v(R) \cdot R^3 \cdot P_{sph}(q,R) \cdot dR \tag{4}$$

$$P_{sph}(q,R) = F^2{}_{sph}(q) = \left[3 \frac{\sin(qR) - qR\cos(qR)}{(qR)^3} \right]^2 \tag{5}$$

with c_v a constant, q the reciprocal space momentum transfer modulus, defined as $q=4\ \pi\ \sin(\Theta)/\lambda$, and R the radius of the spheres.

Results and discussion

The nanoparticles were prepared by aqueous alkaline hydrolysis in combination with a surface functionalization with the tripeptide glutathione (GSH). They were isolated by centrifugation as dried solid and also analyzed in colloidal dispersion. HRTEM images (Figure 1) showed a mostly spherical shape of all glutathione-coated metal oxide nanoparticles with average diameters between 1.5 and 2 nm. No conclusive micrographs could be acquired for the ruthenium-based ultrasmall nanoparticles because the visualization contrast depends on the support thickness, the nanoparticle size, and the atomic scattering factors. Note that ruthenium (Z=44) is the lightest element among the six platinum group metals. Furthermore, the presence of oxygen strongly reduced the density (by a factor of about 2) and thereby the electron contrast.

The HRTEM images were analyzed by a machine-learning algorithm that separated the particles from the background and identified the individual particles. This analysis gave geometric data for all nanoparticle populations, i.e. the minimum Feret diameter, the equivalent diameter, and the sphericity as well as the particle size distribution.

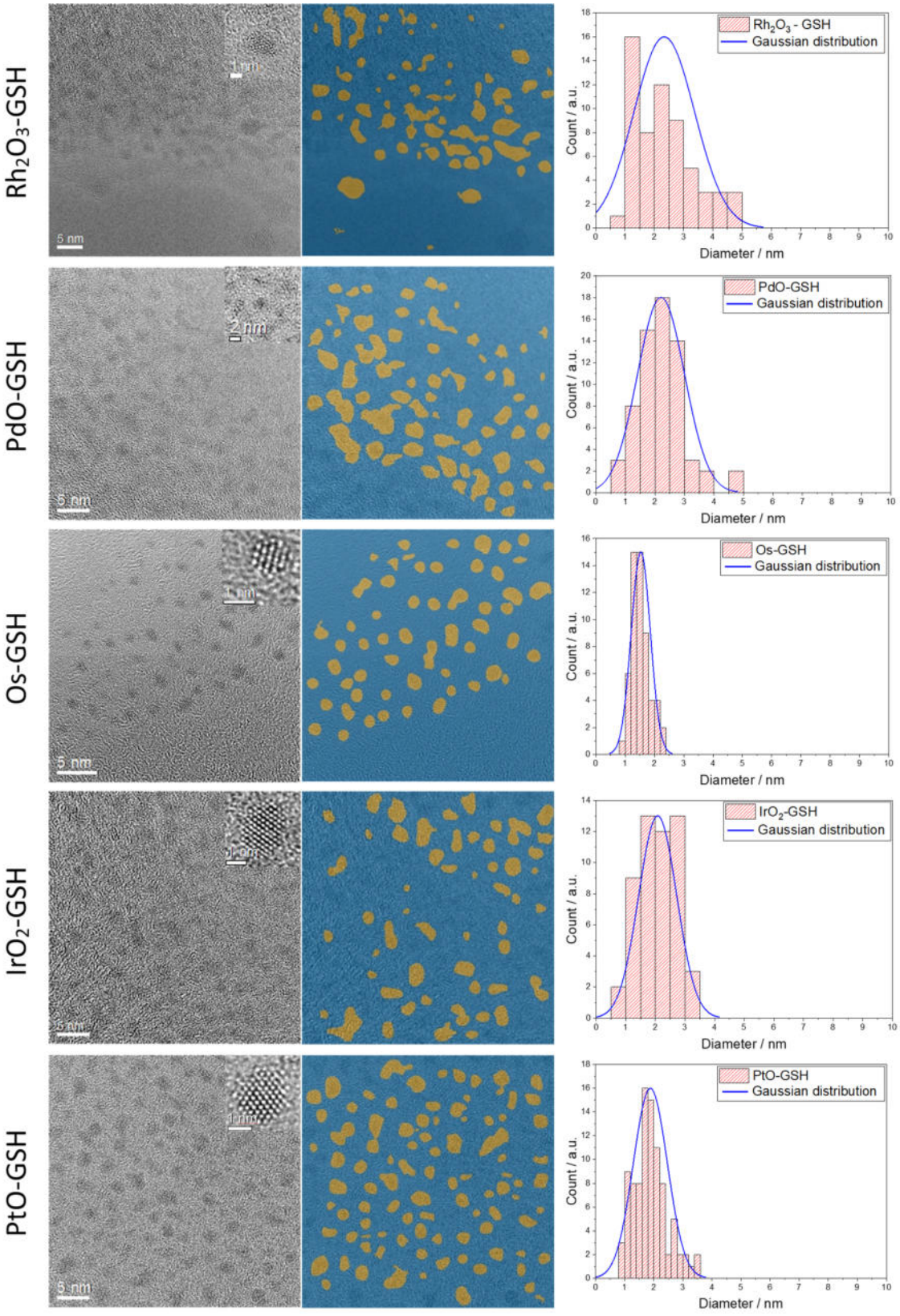
Rh2O3-GSH
PdO-GSH
Os-GSH
IrO2-GSH
PtO-GSH
5 nm
1 nm
2 nm
Rh2O3 - GSH
PdO-GSH
Os-GSH
IrO2-GSH
PtO-GSH
Gaussian distribution
Count / a.u.
Diameter / nm

Figure 1: HRTEM images of glutathione-coated nanoparticles with machine-learning particle classification and particle size distribution analysis (equivalent diameter). The particles are mostly monodisperse with a high degree of internal crystallinity.

The particle diameter by HRTEM was in good agreement with results by small-angle X-ray scattering (SAXS) that also probes the electron-dense inorganic core (Figure 2). Neither larges particles nor significant agglomeration were observed by SAXS.

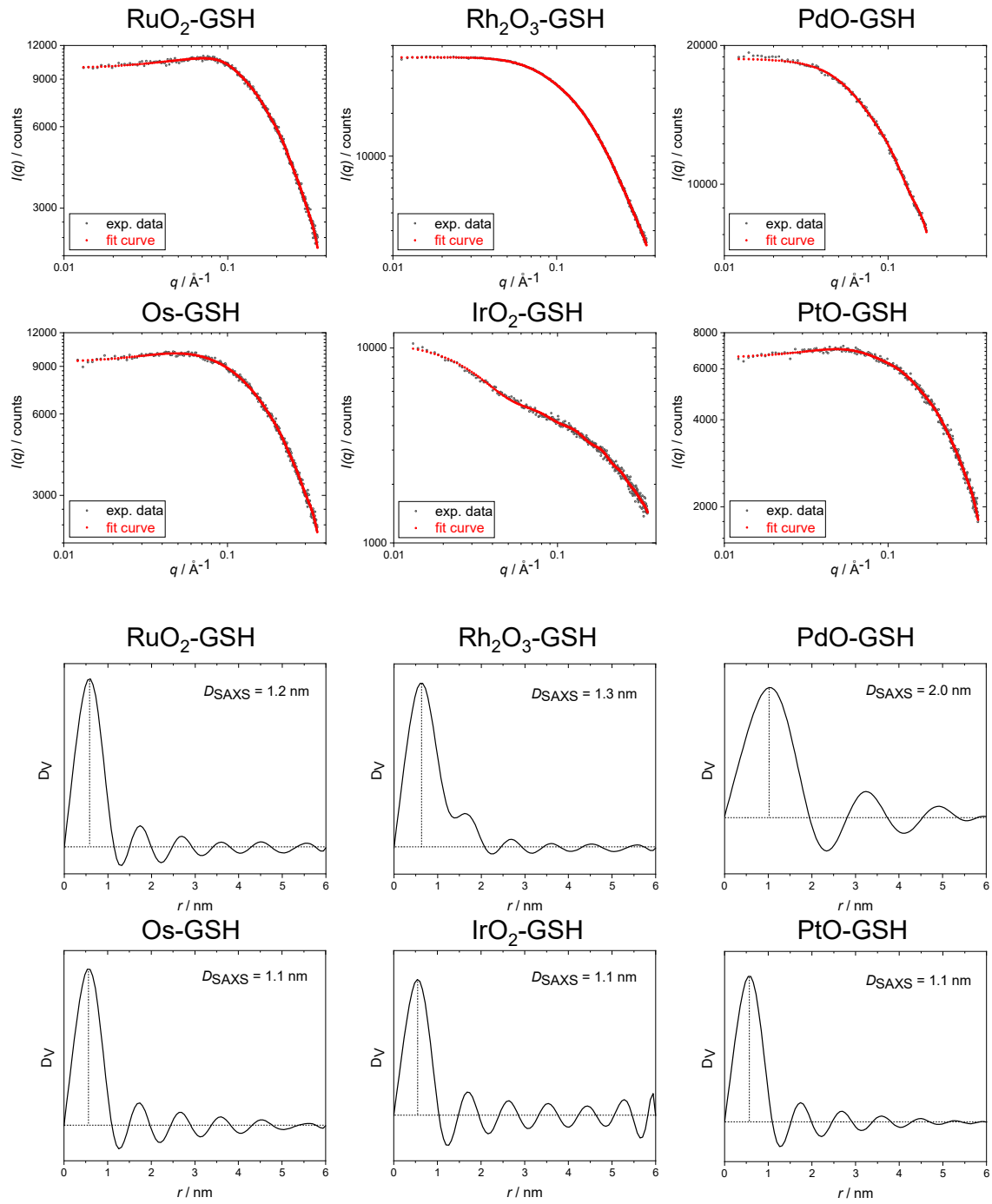

Figure 2: Small-angle X-ray scattering results of water-dispersed glutathione-coated nanoparticles with experimental data *I(q)* and model fit (**top**), and the volume-weighed particle size distribution *Dv* with determined diameters D_{SAXS} (**bottom**). The metal oxide nanoparticles were well dispersed without visible agglomeration. Note that SAXS probes the inorganic (metal oxide) core only, i.e. the organic shell remains invisible.

HRTEM and SAXS both probe the nanoparticle core. To elucidate the contribution of the ligand shell, other methods need to be employed. Differential centrifugal sedimentation (DCS) gives the hydrodynamic diameter of dispersed particles during sedimentation (Figure 3). All particles were well dispersed and did not agglomerate. The diameter was comparable to the diameters from HRTEM and SAXS. Note that the hydrodynamic diameter of small nanoparticles is systematically underestimated by DCS due to the lower effective density of the conjugate of the dense metal core and the light ligand shell. For the evaluation of the DCS data, an average particle density must be assumed. This is lower than the density of the pure metal/metal oxide and basically unknown. In the calculation where the density of the metal oxide is assumed, it leads to an apparently lower particle diameter because the shell slows down the sedimentation rate, mimicking a smaller particle.[35]

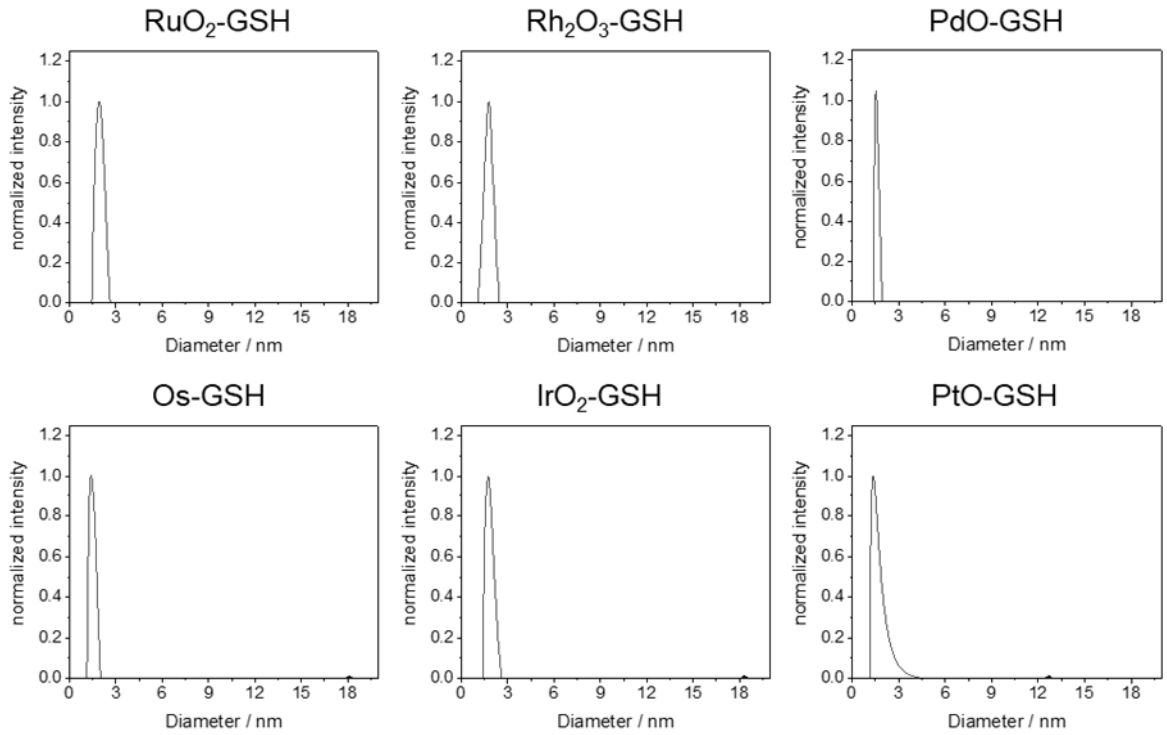

Figure 3: Particle size distribution of water-dispersed glutathione-coated metal oxide nanoparticles as determined by differential centrifugal sedimentation (DCS). All particles have a monomodal size distribution, and no agglomerated particles were found.

Another method to probe the hydrodynamic diameter is ^{1}H-DOSY NMR spectroscopy that is possible for ultrasmall nanoparticles.[14, 36-38] The Stejskal-Tanner plots (Figure 4) gave diffusion coefficients from which hydrodynamic diameters were derived. As expected, the hydrodynamic diameter by DOSY was larger than the diameter of the metal core determined by SAXS due to the hydrated ligand shell by about 0.2 to 0.4 nm. There was no indication for dissolved (i.e. unbound) glutathione that would have a higher diffusion coefficient.

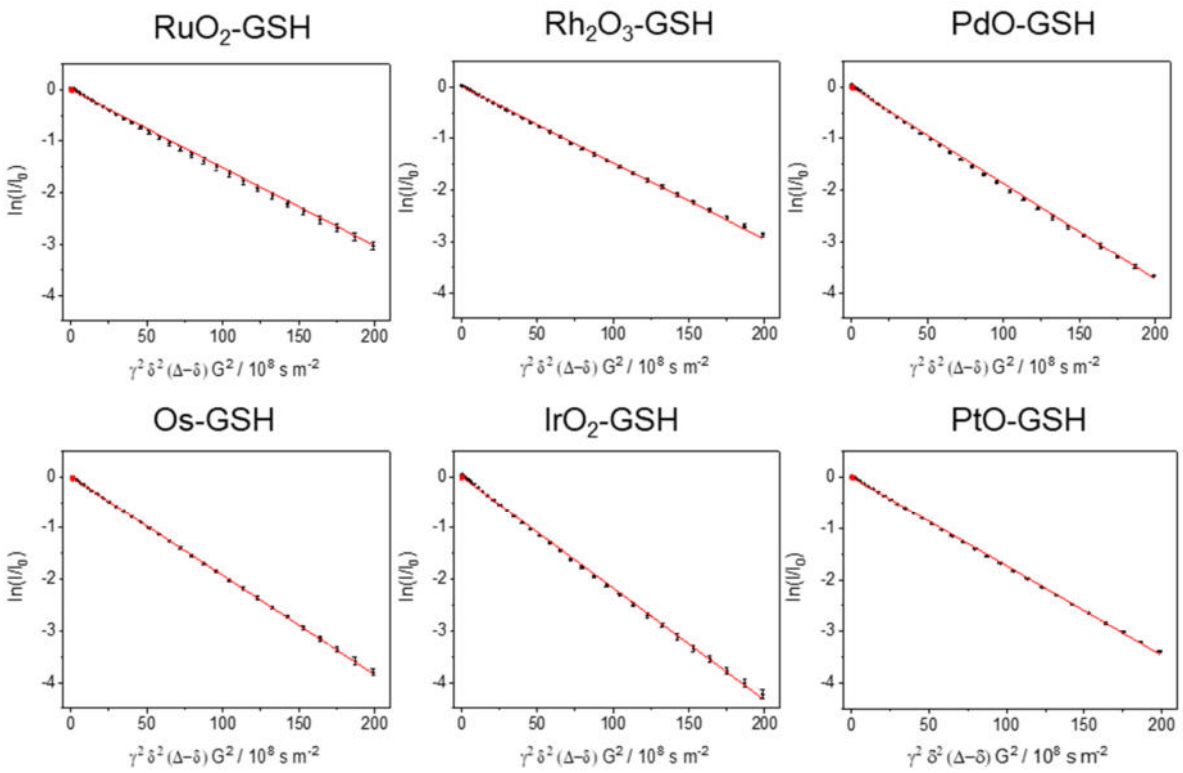

Figure 4: Stejskal-Tanner plots of ^{1}H-DOSY NMR data of glutathione-coated nanoparticles. Data points are the average of all analyzed ^{1}H signals, and the error bars represent the standard deviation of the mean. The negative slope equals the translational diffusion coefficient. DOSY probes the hydrodynamic diameter of dispersed particles, i.e. the metal oxide core and the glutathione shell together.

All particles showed an absorption in the near-UV range without particular features (Figure 5). None of the particles was autofluorescent as probed by an UV lamp. There was no indication for plasmon resonance, i.e. there were no large metal particles that could have been formed as side product (metal oxide particle do not give a plasom resonance).

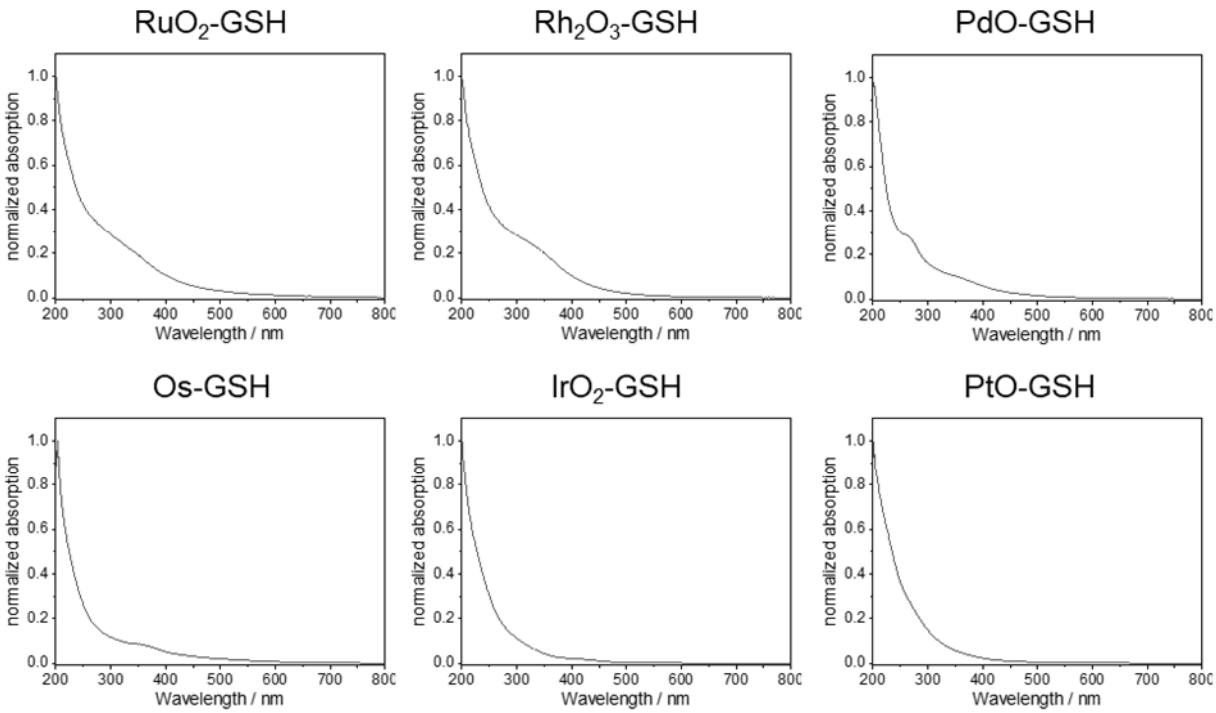

Figure 5: Optical properties of glutathione-coated nanoparticles as determined by UV/VIS spectroscopy. No plasmon resonance of larger metallic nanoparticles (possible side product) is seen in the visible range of the spectrum.

The chemical nature of the nanoparticles cannot be determined by particle size analyses. In contrast, some methods like DCS require the particle density and therefore their chemical nature. Therefore, the electronic structure and the oxidation state of the nanoparticles were determined by X-ray photoelectron spectroscopy (XPS). Figure 6 and Table 1 give the results for all metal oxide cores.

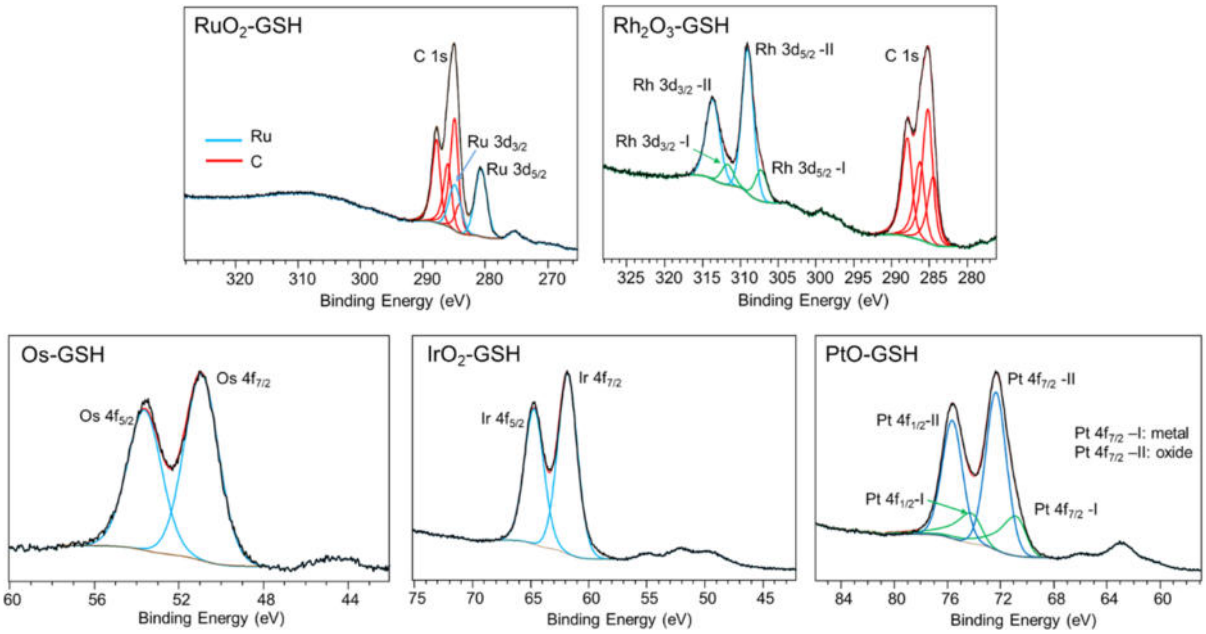

Figure 6: High-resolution XPS data of the metals of glutathione-coated nanoparticles. Palladium was reduced during the XPS measurement; therefore it was not possible to record a spectrum. The colored fit curves represent different carbon species (red), and the spin-orbit pairs of the metallic and/or oxidic species. The metallic species are labelled with I, the oxides with II. Except for osmium, all particles consist of oxides.

Table 1: Detailed summary of the XPS data of the core of glutathione-coated metal oxide nanoparticles.

photoelectron	ruthenium	rhodium		palladium	
$3d_{5/2}$ / eV	280.8	309.0	307.3	-	
$3d_{3/2}$ / eV	284.9	313.7	311.7		
photoelectron	osmium	iridium		platinum	
$4f_{7/2}$ / eV	50.9	61.8		70.4	72.3
$4f_{5/2}$ / eV	53.6	64.7		73.7	75.7

In the case of ruthenium, the $3d_{3/2}$ signal overlapped with the C1s signal, therefore only the $3d_{5/2}$ signal could be evaluated. A binding energy of 280.2 eV is expected for metallic ruthenium and 280.7 eV for RuO_2,[39] indicating an oxidation state of +IV. Two different Rh $3_{d5/2}$ species with binding energies of 307.3 eV and 309.0

eV were found for rhodium. The comparison with literature values for metallic rhodium (307.6 eV)[39, 40] and rhodium(+III) oxide (308.8 eV)[41] shows that Rh(0) and Rh(+III) are both present in the particles. Only one Os $4f_{7/2}$ species with a binding energy of 50.9 eV was found for osmium. Reference spectra for various osmium compounds with oxidation states from 0 to +VI show a binding energy of 50.6 eV for Os(0) and 51.7 eV for Os(+II).[42] The binding energy obtained for the particles is therefore between these two values, being significantly closer to Os(0). In the case of purely metallic osmium, two well-separated sharp signals for Os $4f_{7/2}$ and Os $4f_{5/2}$ are expected.[42] However, the XP spectrum of the Os-GSH particle showed two broad peaks that overlap, suggesting a partially oxidized state of osmium. For IrO_2-GSH, a binding energy of 61.8 eV for Ir $4f_{7/2}$ was determined in the XP spectrum. This is in line with earlier data on porous Ir/IrO_2 superstructures (61.7/64.5 eV).[43] Ultrasmall platinum nanoparticles contained two species of Pt $4f_{7/2}$. The first species with a binding energy of 70.4 eV had a lower value than expected for metallic platinum (71.2 eV). This is in agreement with a previously reported binding energy of 2-3 nm-sized PVP-coated platinum particles.[44] This effect was explained by a charge transfer from PVP to Pt. The main species with a proportion of 73% in the PtO-GSH particle has a binding energy of 72.3 eV, corresponding to a Pt(+II) state as in PtO.[44]

The crystallographic nature of the nanoparticles was determined by X-ray powder diffraction. Although the particles were very small, causing extremely broad diffraction peaks, a quantitative analysis by Rietveld refinement was still possible.[10, 19, 45-47] Figure 7 shows the corresponding diffractograms.

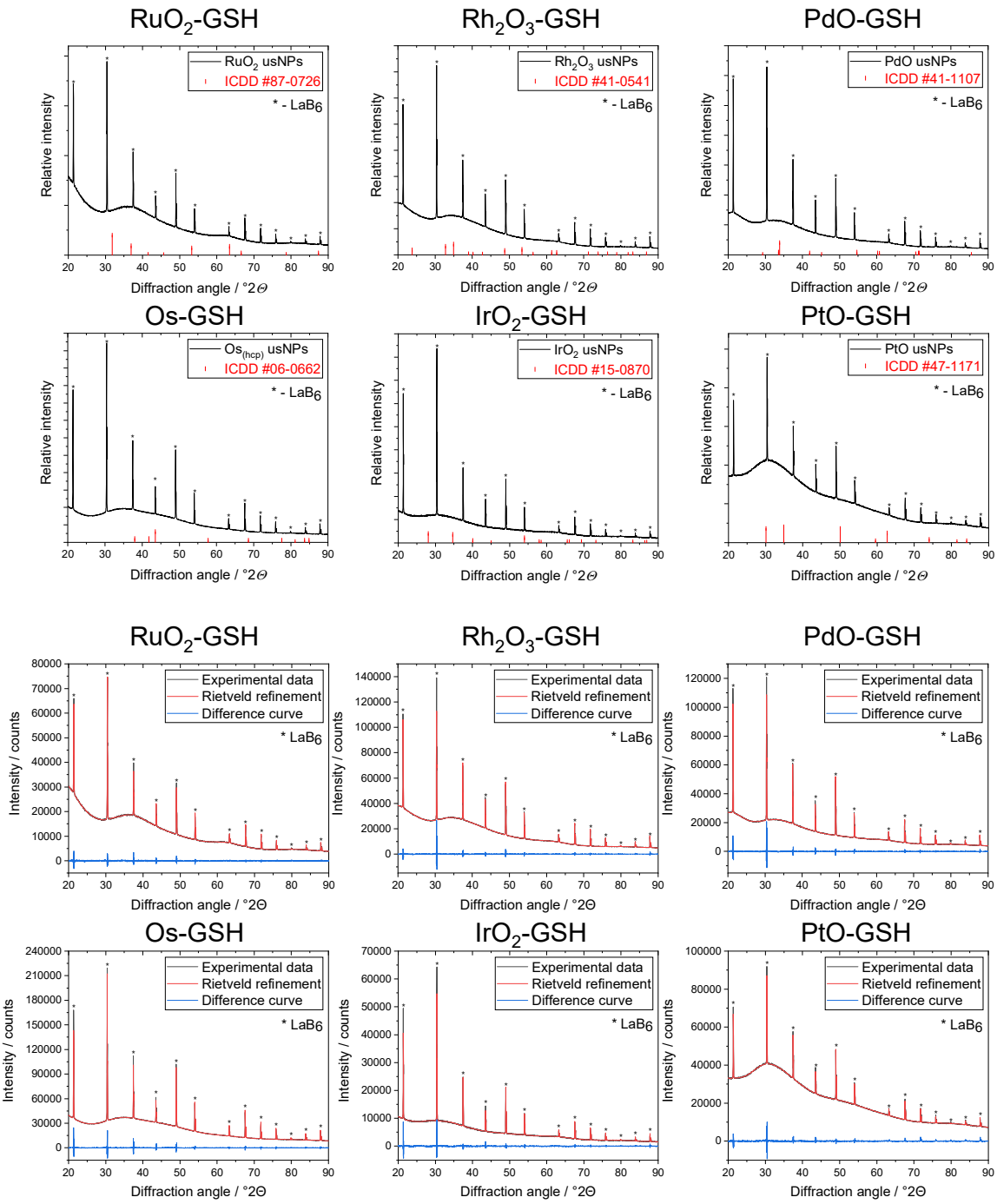

Figure 7: X-ray powder diffractograms of glutathione-coated nanoparticles with qualitative phase analysis (**top**) and Rietveld refinement (**bottom**). The sharp peaks all belong to the standard LaB_6. The very broad diffraction peaks of the metal oxides showed up as broad humps. Except for osmium, all particles consisted of oxides.

The nanoparticles were all crystalline oxides except for osmium. We want to stress that Rietveld fits with the structures of the pure metals failed in all cases, except for osmium. Despite the small particle size, causing extremely broad diffraction peaks, it was possible to identify the crystal systems by Rietveld analysis and to estimate the crystallite size from peak broadening. The fact that the crystallites had a size similar to the particles indicates mostly single-crystalline particles. This agrees with the HRTEM images which showed mostly single-crystalline particles (Figure 1).

Fast Fourier transform (FFT) analysis of HRTEM images was possible of single particles of the heavy platinum group metals (Os, Ir, Pt). For the light platinum group metals (Ru, Rh, Pd), the electron density of the ultrasmall nanoparticles was not sufficient to obtain reasonable FFT patterns. For osmium, we found the diffraction peaks of elemental osmium. For iridium, we found mainly the diffraction peaks of iridium dioxide (IrO_2). For platinum, we found the diffraction peaks of Pt (Figure 8). It must be noted that the high electron flux encountered by the particles in the HRTEM may change their chemical composition, especially as they are ultrasmall and have a high number of surface atoms. Thus, the FFT data have to be taken with some care. However, as they are in line with the results by X-ray powder diffraction and X-ray photoelectron spectroscopy, we can tentatively accept them as supportive.

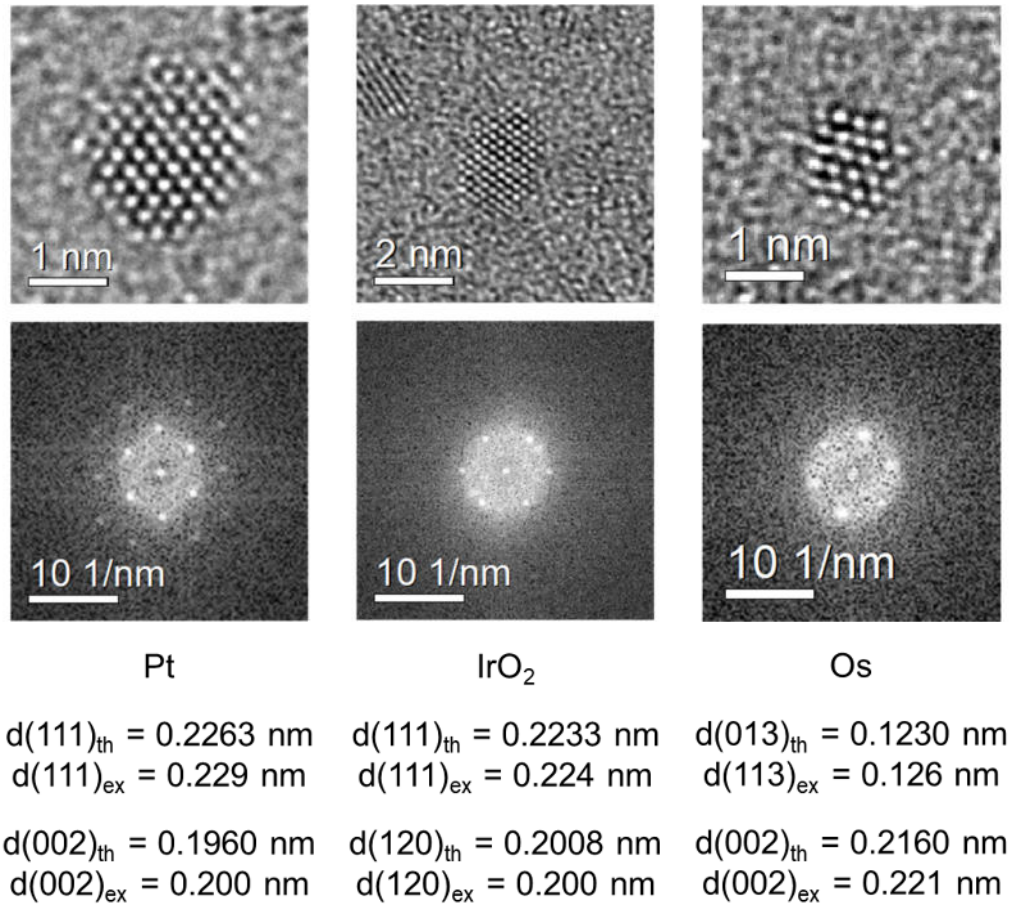

Figure 8: HRTEM images of single nanoparticles and the corresponding fast Fourier transform (FFT) patterns with theoretical and experimental *d*-spacings. All particles were crystalline as shown by the electron diffraction images.

The hydrolytic synthesis occurred mostly without change of the oxidation state of the metal precursor used, despite the presence of the reducing agent $NaBH_4$. In the case of rhodium, $RhCl_3$ (+III) was converted to Rh_2O_3 (still +III). In the case of palladium, $Pd(NO_3)_2$ (+II) was converted to PdO (still +II). In the case of iridium, Na_2IrCl_6 (+IV) was converted to IrO_2 (still +IV). In contrast, osmium was mostly reduced from H_2OsCl_6 (+IV) to elemental osmium with about 20% remaining OsO_2 (+IV). Platinum was mostly reduced from H_2PtCl_6 (+IV) to PtO (+II). Only ruthenium was oxidized from +III ($RuCl_3$) to +IV (RuO_2). This indicates the delicate balance between oxidation/reduction and hydrolysis during the synthesis. A fully oxidized metal core (Ag^+) was found earlier for glutathione-

coated silver nanoparticles by XPS.[19] However, we also clearly found the fcc structure of elemental silver by XRD. It was impossible to match the structure of Ag_2O with the diffraction data.[19] For cysteine-coated ultrasmall gold nanoparticles, we found about 5% of Au(I) and 95% of Au(0) by XPS and the gold fcc structure by XRD.[14] For PVP-coated iridium/iridium dioxide superstructures we found a ratio of Ir(0) to Ir(+IV) of 2:1 by XPS.[43] The question why osmium alone was almost fully reduced to the metal in contrast to the other metals cannot yet be answered; it is obviously the effect of the applied reaction conditions which were more or less identical for all metals. The fact that we have a rapid synthesis of ultrasmall nanoparticles which are probably not in thermldynamic equilibrium states suggests that the see the result of both thermodynamic and kinetic factors which are different for each metal.

Table 2 gives the numerical results for all nanoparticles. In summary, they are all present as individual and well-dispersed particles in aqueous solution.

Table 2: Particle size properties of glutathione-coated metal oxide nanoparticles by HRTEM, SAXS, XRD, and DCS. Standard deviations of the last digits are given in parentheses. We estimate the accuracy of DOSY and DCS data to 0.2 nm. For Os-GSH, the density of elemental osmium was assumed for the calculation.

	RuO_2-GSH	Rh_2O_3-GSH	PdO-GSH	Os-GSH	IrO_2-GSH	PtO-GSH
DCS: Hydrodynamic diameter / nm	1.9(2)	1.8(2)	1.5(2)	1.4(2)	1.7(2)	1.6(2)
^{1}H-NMR DOSY: Diffusion coefficient / 10^{-10} m^2 s^{-1}	1.6(2)	1.5(2)	1.9(2)	1.9(2)	2.2(2)	1.7(2)
^{1}H-NMR DOSY: Hydrodynamic diameter / nm	2.5(2)	2.7(3)	2.1(2)	2.0(2)	1.8(2)	2.2(3)
HRTEM: Particle core diameter / nm	-	1.8(7)	2.0(4)	1.5(2)	1.6(4)	1.8(3)
HRTEM: Average equivalent diameter	-	2.3(10)	2.2(8)	1.5(3)	2.0(6)	1.9(6)
HRTEM: Average minimum Feret diameter	-	2.0(9)	1.9(7)	1.4(3)	1.8(5)	1.7(5)
HRTEM: Average sphericity	-	0.8(2)	0.8(2)	0.9(1)	0.9(1)	0.9(1)
SAXS: Particle core diameter / nm	1.2(1)	1.3(1)	2.0(2)	1.1(1)	1.1(1)	1.1(1)
XPS (metal)	Ru(+IV)	Rh(0), Rh(+III)	-	Os(0), Os(+II)	Ir(+IV)	Pt, Pt(+II)
Electron diffraction	-	-	-	Os	IrO_2	Pt
XRD: Crystallite size / nm	1.0(2)	1.1(4)	1.4(3)	Os: 0.8(1) OsO_2 0.4(2) Os (hcp): ≈80%	1.3(3)	0.9(1)
XRD: Lattice parameters / Å	cubic RuO_2 *a*=4.90(2)	rhombohedral Rh_2O_3 *a*=5.13(3) *c*=13.92(15)	tetragonal PdO *a*=3.07(4) *c*=5.18(15)	*a*=2.73(1) *c*=4.32(4) tetragonal OsO_2 ≈20% *a*=4.5(1) *c*=3.2(1)	tetragonal IrO_2 *a*=4.50(3) *c*=3.17(3)	cubic PtO *a*=5.15(3)

Next, we investigated the nature of the glutathione ligand shell by NMR spectroscopy. Figure 9 shows ^{1}H-NMR spectra of dissolved glutathione and of dispersed nanoparticles.

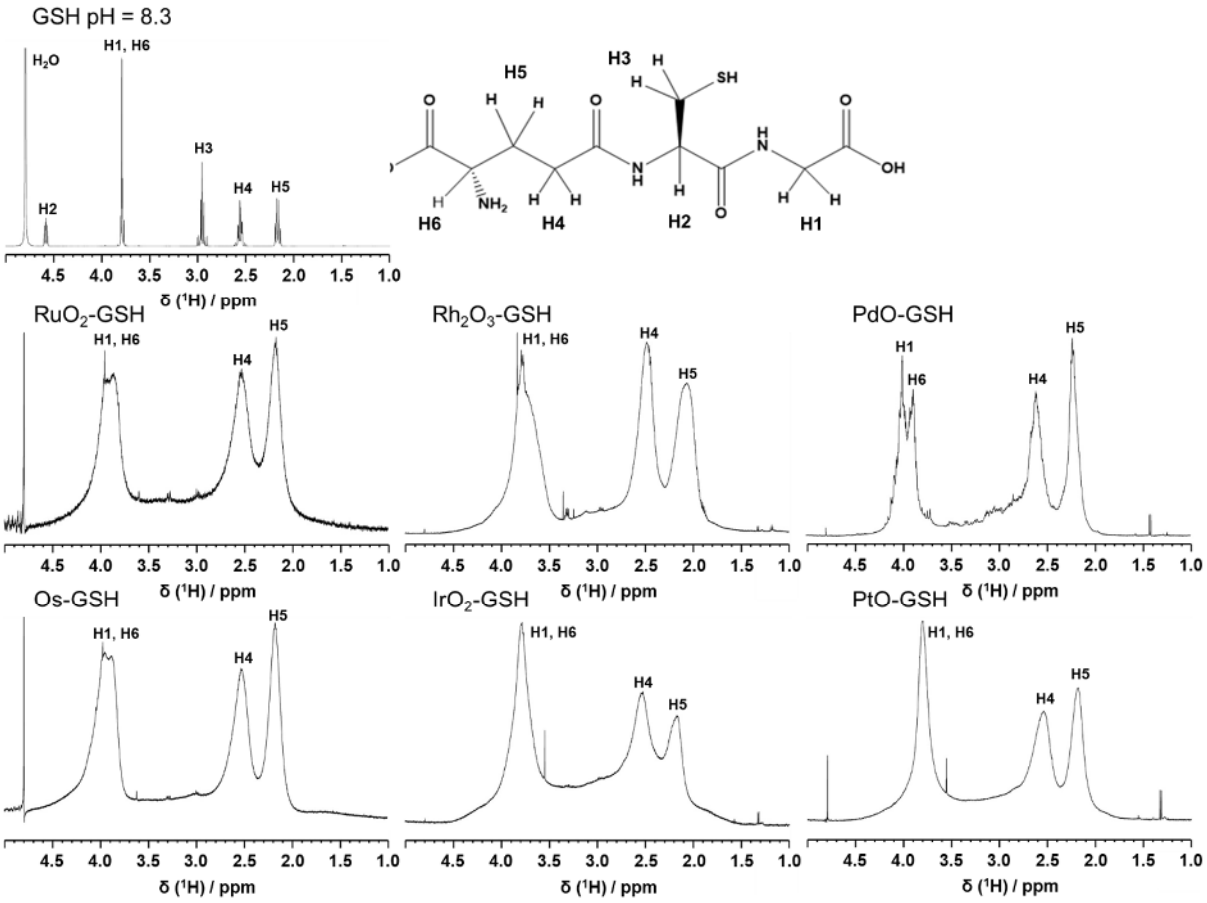

Figure 9: ^{1}H-NMR spectra of dissolved glutathione and of water-dispersed glutathione-coated nanoparticles at pH 8-9. The proton assignment was also based on results from 2D NMR spectroscopy (see Supplementary Information). The glutathion ligand is present in all cases, but the presence of the metal oxide core leads to strongly broadened and shifted NMR peaks.

All ^{1}H-NMR spectra showed strongly broadened signals for the bound glutathione that were assigned to the protons, taking into account our earlier data on ultrasmall silver[19] and gold nanoparticles[12, 48] with a glutathione shell. The absence of sharp signals confirmed the absence of dissolved or detached molecular glutathione. In

general, the NMR spectra were very similar for the six metals. The H2 signal was not detectable due to its vicinity to the water suppression (4.6 ppm).[19] In comparison to ultrasmall silver and gold nanoparticles[19, 48] it is remarkable that the H3 signal (found at 3.4 ppm for silver/gold-conjugated glutathione[12]) was not detectable with any platinum group metal. Note that the H3 protons (Cys Hβ) were not visible in Au-KCD nanoparticles either.[11] Furthermore, the line width of H4 and H5 resonances was larger than with silver and gold, resulting in a loss of the splitting into triplets due to J-coupling.[19, 48]

As the particle size is similar for nanoparticles of silver, gold, and platinum group metals (1.5 to 2 nm), the particularly broad peaks can probably be explained by electronic effects. Group 11 metals like gold and silver have a full d-shell whereas platinum group metals have an open d-shell with different numbers of unpaired electrons, depending on the metal and its oxidation state. This will interfere with the NMR spectra and cause line broadening like paramagnetic ions. This is obviously the case for metal oxides.

Figure 10 shows ^{13}C-NMR spectra of water-dispersed nanoparticles. These were again comparable for the six metals and underline the structural integrity of the GSH ligand. The peaks of the carbon atoms close to the gold surface (C2 and C3) were not detectable in Ag-GSH nanoparticles.[19] The line-broadening effect of the metal was also observed in 2D NMR spectroscopy (see Supporting Information, Figures S1 to S3). In summary, there was no indication from NMR spectroscopy that the chemical nature of the GSH ligand was changed by the surface conjugation. We also did not see sharp peaks that would indicate "free" (dissolved) glutahtione. This indicates that the bond between metal oxide nanoparticle and glutathione is strong and comparable to the bond to a metallic nanoparticle (see Ref.[19] where we have reported variable temperature experiments for ultrasmall silver-glutathione nanoparticles which were stable in water at least up to 85 °C).

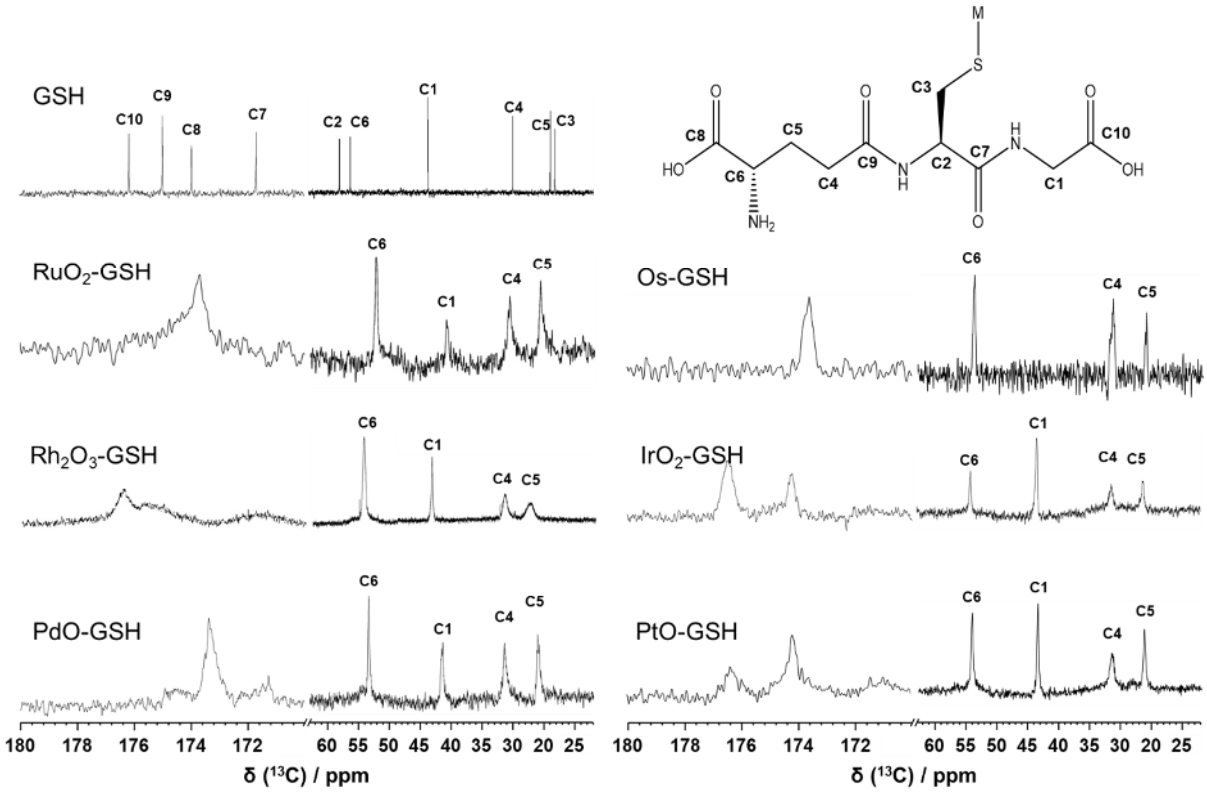

Figure 10: ^{13}C-NMR spectra of dissolved glutathione and of water-dispersed glutathione-coated nanoparticles (all recorded at pH 8.3), showing the integrity of the GSH ligand on the nanoparticle surface.

The number of GSH ligands on each nanoparticle was determined by quantitative ^{1}H-NMR spectroscopy. Based on the signal intensities of GSH (H1, H3, H4, H5, and H6 protons, i.e. the intensity of 9 protons) and of maleic acid in combination with the metal concentration in the dispersion, the number of ligands was computed. The metal concentration together with the assumption of a core diameter of 1.8 nm gives the concentration of spherical nanoparticles. Table 3 gives all analytical data of the nanoparticles including their ligand shells. For comparison, the molecular footprint of GSH on silver nanoparticles (2 nm) was 0.08 nm^2,[19] on gold nanoparticles (2 nm) it was 0.10 nm^2,[12] and for cysteine on gold nanoparticles (1.78 nm) it was 0.15 nm^2,[14] in line with the results for the

metal oxide nanoparticles. It is noteworthy that the mass fraction of GSH in all cases exceeded the mass fraction of the inorganic core.

Table 3: GSH shell of the metal oxide nanoparticles, based on an average particle diameter of 1.8 nm and the assumption of spherical nanoparticles. The given stoichiometries of the oxides were used together with the density of the bulk oxide phases, except for osmium where we used the values for metallic osmium. M(GSH)=307.33 g mol^{-1}.

	RuO_2-GSH	Rh_2O_3-GSH	PdO-GSH	Os-GSH	IrO_2-GSH	PtO-GSH
Measured metal concentration (AAS or ICP-MS) / g L^{-1}	0.114	1.296	1.350	0.613	0.608	0.823
Calculated metal oxide concentration / g L^{-1}	0.150	1.498	1.553	-	0.709	0.890
Measured GSH concentration (NMR) / g L^{-1}	0.237	3.359	3.663	1.998	1.692	1.613
Weight ratio GSH to metal oxide	1.579	2.101	2.359	3.260	2.385	1.811
Particle density / g cm^3	6.97	8.2	8.3	22.59	11.66	14.17
Particle core volume / nm^3	3.052	3.052	3.052	3.052	3.052	3.052
Particle core weight / g·10^{-20}	2.127	2.503	2.533	6.895	3.559	4.325
Molar mass per nanoparticle core / g mol^{-1}	12,810	15,080	15,260	41,530	21,440	26,050
Nominal chemical composition nanoparticle core	$Ru_{96}O_{192}$	$Rh_{119}O_{178}$	$Pd_{125}O_{125}$	$Os_{211}O_{84}$	$Ir_{96}O_{192}$	$Pt_{123}O_{123}$
Particle concentration / L^{-1}	$7.05\cdot10^{18}$	$5.98\cdot10^{19}$	$6.13\cdot10^{19}$	$8.89\cdot10^{18}$	$1.99\cdot10^{19}$	$2.06\cdot10^{19}$
m(GSH) per particle / g·10^{-20}	3.361	5.259	5.975	2.247	8.489	7.834
n(GSH) per particle / mol·10^{-22}	1.094	1.711	1.944	7.313	2.762	2.549
GSH molecules per nanoparticle	66	103	117	440	166	153
Overall composition of one nanoparticle	$Ru_{96}O_{192}(GSH)_{66}$	$Rh_{119}O_{178}(GSH)_{103}$	$Pd_{125}O_{125}(GSH)_{117}$	$Os_{211}O_{84}(GSH)_{440}$	$Ir_{96}O_{192}(GSH)_{166}$	$Pt_{123}O_{123}(GSH)_{153}$
Total molecular mass of one nanoparticle / g mol^{-1}	33,070	46,700	51,180	176,610	72,400	73,020
Particle core surface area / nm^2	10.2	10.2	10.2	10.2	10.2	10.2
Molecular footprint per GSH molecule / nm^2	0.155	0.099	0.087	0.023	0.061	0.066

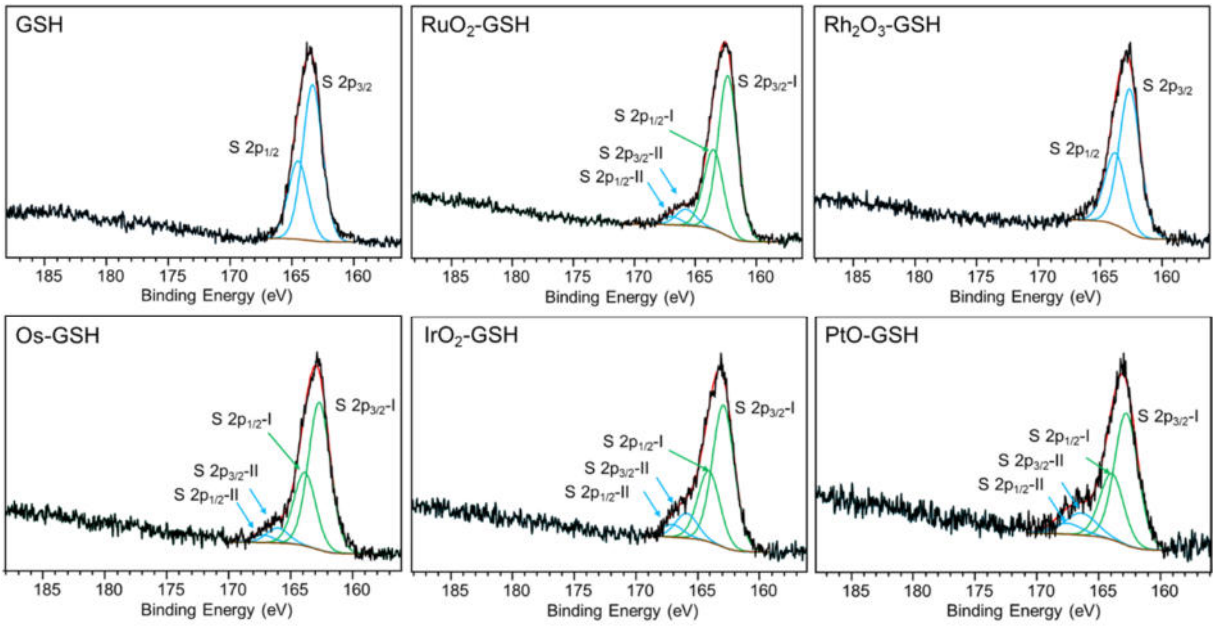

Figure 11: XPS data of the S 2p photoelectrons of glutathione-coated metal oxide nanoparticles. The colored fit curves represent the spin-orbit pairs S $2p_{3/2}$ and S $2p_{1/2}$ of different sulfur species labelled I and II. In all cases, sulfur is present as deprotonated thiolate group, confirming the binding to the metal oxide core.

The binding energies of sulfur of the glutathione capping agent were determined by XPS to get insight into the binding situation (Figure 11 and Table 4). Except for rhodium, two species of sulfur were found for all particle systems, each with two $S2p_{1/2}$ and $S2p_{3/2}$ signals (in contrast to Ag-GSH nanoparticles where only one signal for sulfur was found at 162 eV)[19]. The binding energies of all particle systems were in a comparable range with 162.3 eV (ruthenium) to 162.9 eV (iridium). This points to a deprotonated thiolate group of the glutathione ligand in all cases as with glutathione-coated silver nanoparticles.[19] The signal at 165.8 eV indicates an oxidized sulfur species.[49]

Table 4: Detailed XPS data of glutathione-coated metal oxide nanoparticles of $S2p_{3/2}$ and $S2p_{1/2}$ photoelectrons.

Photoelectron	RuO_2-GSH		Rh_2O_3-GSH		GSH	
	B_E / eV	at / %	B_E / eV	at / %	B_E / eV	at / %
$S2p_{3/2}$ -I	162.3	91	162.6	100	163.3	100
$S2p_{1/2}$ -I	163.5		163.8		164.5	
$S2p_{3/2}$ -II	165.8	9				
$S2p_{1/2}$ -II	167.0					
Photoelectron	Os-GSH		IrO_2-GSH		PtO-GSH	
	B_E / eV	Fraction / %	B_E / eV	Fraction / %	B_E / eV	Fraction / %
$S2p_{3/2}$ -I	162.7	91	162.9	85	162.8	82
$S2p_{1/2}$ -I	163.9		164.1		163.9	
$S2p_{3/2}$ -II	166	9	165.9	15	166.4	18
$S2p_{1/2}$ -II	167.2		167.1		167.6	

XP spectra at the N 1s edge are shown in Figure 12 and Table 5. Pure glutathione shows two XPS signals at 399.8 eV (intensity 74%; two amide nitrogens) and 401.2 eV (intensity 26%; one amine nitrogen). In the nanoparticles, the peak at 401.2 eV has split into one at 398 and one at 401.4 eV. This may indicate a binding of this amine group to the surface of the metal oxide nanoparticle which appears possible via an oxide-amine interaction.

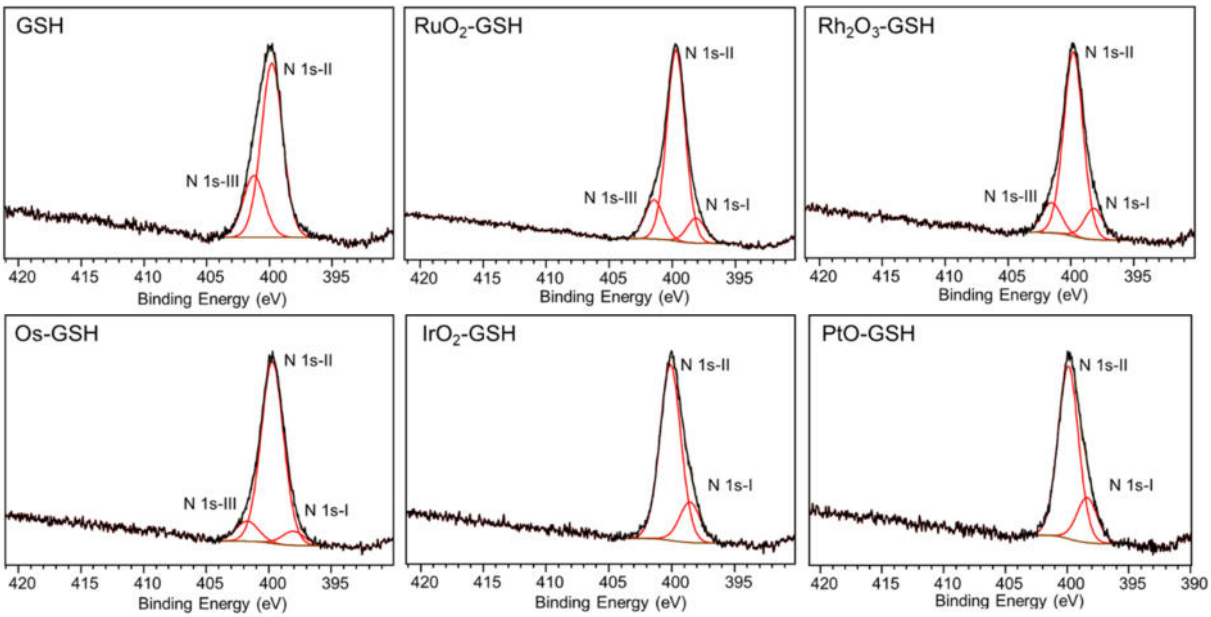

Figure 12: N 1s high resolution XPS data of glutathione-coated metal oxide nanoparticles. The colored fit curves represent different N species labelled I, II, and III. Besides nitrogen in amide as expected, the amino group is split, indicating a back-binding to the nanoparticle surface.

Table 5: Detailed XPS data of N1s photoelectrons of glutathione-coated metal oxide nanoparticles. For pure glutathione, we observed a major peak at 399.8 eV and a minor peak at 401.2 eV.[19]

Photoelectron	RuO_2-GSH		Rh_2O_3-GSH		GSH	
	B_E / eV	Fraction / %	B_E / eV	Fraction / %	B_E / eV	Fraction / %
N 1s - I	398.1	10	398.2	13		
N 1s - II	399.7	75	399.8	75	399.8	74
N 1s - III	401.4	15	401.5	12	401.2	26
Photoelectron	Os-GSH		IrO_2-GSH		PtO-GSH	
	B_E / eV	Fraction / %	B_E / eV	Fraction / %	B_E / eV	Fraction / %
N 1s - I	398.0	7	398.6	19	398.4	21
N 1s - II	399.7	84	400.1	81	399.9	79
N 1s - III	401.7	9				

Our results extend earlier data on ultrasmall platinum group metal oxide nanoparticles. Palladium nitrate was hydrolyzed in water and formed palladium(II) oxide nanoparticles with a size of 2.2 nm, as shown by HRTEM, XPS and XRD.[50] Platinum(II) oxide particles were prepared on C_3N_4 nanosheets with a size of 2 nm. The oxidation state was determined by XPS.[51] Ultrasmall PtO_2 nanoparticle were prepared under basic conditions in the presence of protective agents like PVP and carbobetaine. Their size depended on the pH value and the concentration of PVP.[52, 53] Unprotected PtO_2 nanoparticles (1.9 nm) were prepared by hydrolysis of H_2PtCl_6 in boiling water with stabilizing agent.[54] Ultrasmall RuO_2 nanoparticles were synthesized on carbon nanotubes in basic conditions.[55, 56] In general, iridium tends to oxidize in basic conditions, resulting in the formation of ultrasmall IrO_2 particles.[57]

In this work, we have prepared the particles by hydrolysis, followed by colloidal stabilization, using the synthetic pathway of a Brust-Schiffrin synthesis [26, 27]. This is different from classical methods where particles are formed by impregnation of a support.[58] However, the elucidation of the microscopic reaction mechanism which involves alkaline hydrolysis under reducing conditions ($NaBH_4$) in the presence of a metal-coordinating ligand (glutathione) must be left to future studies. When it comes to an application in heterogeneous catalysis, the presence of the ligand on the particle surface (here: glutathione) may change the catalytic properties.[59] Clearly, such oxidic particles will change under catalytic conditions in any case. This remains to be studied in practice, also after synthesis on a larger scale, but it can be concluded that this liquid-phase hydrolysis offers a pathway to well-defined ultrasmall particles.

Conclusions

Ultrasmall nanoparticles of platinum group metals can be prepared by a straightforward hydrolysis reaction from aqueous precursors, i.e. their metal salts.

The surface is terminated by the capping agent glutathione that prevents their crystal growth to a final diameter between 1 and 2 nm. Due to their small size, the ligand shell of particles can be well analyzed by NMR spectroscopy. The metallic core diameter is visualized by transmission electron microscopy, followed by automated image analysis by machine learning. The combination of X-ray powder diffraction and X-ray photoelectron spectroscopy, combined with electron diffraction, proves the oxidic character of the nanoparticles. It should be emphasized that without these methods, the particles would probably have been assumed to be metallic in nature. Neither colloid-chemical methods nor imaging by TEM would have shown their oxidic nature. This underscores the need to apply a range of different methods to characterize such ultrasmall particles. With respect to the binding of the capping ligand, it can be clearly stated that its chemical nature has not been changed (by NMR) and that the binding occurs with a thiolate group. However, the exact nature of the nanoparticle-ligand interface cannot be elucidated, probably also due to the fact that each particle is not chemically, structurally and electronically homogeneous. It may well be that the surface has a structure and composition different from the inner core.

Supporting Information

^{1}H-^{1}H-COSY NMR spectra, ^{1}H-^{13}C-HSQC NMR spectra, and ^{1}H-^{13}C-HMBC NMR spectra of glutathione-coated metal oxide nanoparticles.

Acknowledgements

The authors acknowledge financial support by the Deutsche Forschungsgemeinschaft (DFG) in the framework of the Collaborative Research Center SFB 1093: Supramolecular Chemistry on Proteins. We thank Beate Römer and Robin Meya for elemental analyses. Sebastian Leiting (MPI Kohlenforschung,

Mülheim) is gratefully acknowledged for XPS measurements. We thank Dr Felix Niemeyer and Dr Torsten Schaller for NMR measurements.

References

1. Cao, S. W.; Tao, F.; Tang, Y.; Li, Y. T.; Yu, J. G., Size- and shape-dependent catalytic performances of oxidation and reduction reactions on nanocatalysts. *Chem. Soc. Rev.* **2016,** *45*, 4747-4765.
2. Gao, C. B.; Lyu, F. L.; Yin, Y. D., Encapsulated metal nanoparticles for catalysis. *Chem. Rev.* **2021,** *121*, 834-881.
3. Li, Z. P.; Xu, Q., Metal-nanoparticle-catalyzed hydrogen generation from formic acid. *Acc. Chem. Res.* **2017,** *50*, 1449-1458.
4. Rodrigues, T. S.; da Silva, A. G. M.; Camargo, P. H. C., Nanocatalysis by noble metal nanoparticles: controlled synthesis for the optimization and understanding of activities. *J. Mater. Chem. A* **2019,** *7*, 5857-5874.
5. Vile, G.; Albani, D.; Almora-Barrios, N.; Lopez, N.; Perez-Ramirez, J., Advances in the design of nanostructured catalysts for selective hydrogenation. *ChemCatChem* **2016,** *8*, 21-33.
6. Xie, C. L.; Niu, Z. Q.; Kim, D.; Li, M. F.; Yang, P. D., Surface and interface control in nanoparticle catalysis. *Chem. Rev.* **2020,** *120*, 1184-1249.
7. Zhang, T. J.; Walsh, A. G.; Yu, J. H.; Zhang, P., Single-atom alloy catalysts: structural analysis, electronic properties and catalytic activities. *Chem. Soc. Rev.* **2021,** *50*, 569-588.
8. Liu, L. C.; Corma, A., Metal catalysts for heterogeneous catalysis: From single atoms to nanoclusters and nanoparticles. *Chem. Rev.* **2018,** *118*, 4981-5079.
9. Loza, K.; Heggen, M.; Epple, M., Synthesis, structure, properties, and applications of bimetallic nanoparticles of noble metals. *Adv. Funct. Mater.* **2020**, 1909260.
10. van der Meer, S. B.; Seiler, T.; Buchmann, C.; Partalidou, G.; Boden, S.; Loza, K.; Heggen, M.; Linders, J.; Prymak, O.; Oliveira, C. L. P.; Hartmann, L.; Epple, M., Controlling the surface functionalization of ultrasmall gold nanoparticles by sequence-defined macromolecules. *Chem. Eur. J.* **2021,** *27*, 1451-1464.
11. van der Meer, S. B.; Hadrovic, I.; Meiners, A.; Loza, K.; Heggen, M.; Knauer, S. K.; Bayer, P.; Schrader, T.; Beuck, C.; Epple, M., New tools to probe the protein surface: ultrasmall gold nanoparticles carry amino acid binders. *J. Phys. Chem. B* **2021,** *125*, 115-127.
12. Klein, K.; Loza, K.; Heggen, M.; Epple, M., An efficient method for covalent surface functionalization of ultrasmall metallic nanoparticles by surface azidation, followed by copper-catalyzed azide-alkyne cycloaddition. *ChemNanoMat* **2021,** *7*, 1330-1339.
13. van der Meer, S. B.; Loza, K.; Wey, K.; Heggen, M.; Beuck, C.; Bayer, P.; Epple, M., Click chemistry on the surface of ultrasmall gold nanoparticles (2 nm) for covalent ligand attachment followed by NMR spectroscopy. *Langmuir* **2019,** *35*, 7191-7204.
14. Ruks, T.; Beuck, C.; Schaller, T.; Niemeyer, F.; Zähres, M.; Loza, K.; Heggen, M.; Hagemann, U.; Mayer, C.; Bayer, P.; Epple, M., Solution NMR spectroscopy with isotope-labelled cysteine (^{13}C, ^{15}N) reveals the surface structure of L-cysteine-coated ultrasmall gold nanoparticles (1.8 nm). *Langmuir* **2019,** *35*, 767-778.
15. Zarschler, K.; Rocks, L.; Licciardello, N.; Boselli, L.; Polo, E.; Garcia, K. P.; De Cola, L.; Stephan, H.; Dawson, K. A., Ultrasmall inorganic nanoparticles: State-of-the-art and perspectives for biomedical applications. *Nanomedicine* **2016,** *12*, 1663-1701.
16. Jin, J. C.; Wu, X. J.; Xu, J.; Wang, B. B.; Jiang, F. L.; Liu, Y., Ultrasmall silver nanoclusters: Highly efficient antibacterial activity and their mechanisms. *Biomater. Sci.* **2017,** *5*, 247-257.
17. Zheng, K. Y.; Yuan, X.; Goswami, N.; Zhang, Q. B.; Xie, J. P., Recent advances in the synthesis, characterization, and biomedical applications of ultrasmall thiolated silver nanoclusters. *RSC Adv.* **2014,** *4*, 60581-60596.

18. Shang, L.; Dörlich, R. M.; Trouillet, V.; Bruns, M.; Nienhaus, G. U., Ultrasmall fluorescent silver nanoclusters: protein adsorption and its effects on cellular responses. *Nano Res.* **2012,** *5*, 531-542.
19. Wetzel, O.; Hosseini, S.; Loza, K.; Heggen, M.; Prymak, O.; Bayer, P.; Beuck, C.; Schaller, T.; Niemeyer, F.; Weidenthaler, C.; Epple, M., Metal–ligand interface and internal structure of ultrasmall silver nanoparticles (2 nm). *J. Phys. Chem. B* **2021,** *125*, 5645-5659.
20. Kenzler, S.; Fetzer, F.; Schrenk, C.; Pollard, N.; Frojd, A. R.; Clayborne, A. Z.; Schnepf, A., Synthesis and characterization of three multi-shell metalloid gold clusters Au32(R3P)12Cl8. *Angew. Chem. Int. Ed. Engl.* **2019,** *58*, 5902-5905.
21. Kang, X.; Li, Y. W.; Zhu, M. Z.; Jin, R. C., Atomically precise alloy nanoclusters: Syntheses, structures, and properties. *Chem. Soc. Rev.* **2020,** *49*, 6443-6514.
22. Du, X. S.; Jin, R. C., Atomic-precision engineering of metal nanoclusters. *Dalton Trans.* **2020,** *49*, 10701-10707.
23. Kwak, K.; Lee, D., Electrochemistry of atomically precise metal nanoclusters. *Acc. Chem. Res.* **2019,** *52*, 12-22.
24. Zhao, J. B.; Jin, R. C., Heterogeneous catalysis by gold and gold-based bimetal nanoclusters. *Nano Today* **2018,** *18*, 86-102.
25. Zeng, C. J., Precision at the nanoscale: on the structure and property evolution of gold nanoclusters. *Pure Appl. Chem.* **2018,** *90*, 1409-1427.
26. Brust, M.; Fink, J.; Bethell, D.; Schiffrin, D. J.; Kiely, C., Synthesis and reactions of functionalised gold nanoparticles. *Chem. Commun.* **1995**, 1655-1656.
27. Liz-Marzan, L. M., Gold nanoparticle research before and after the Brust–Schiffrin method. *Chem. Comm.* **2013,** *49*, 16-18.
28. Thust, A.; Barthel, J.; Tillmann, K., FEI Titan 80-300 TEM. *J. Large-scale Res. Fac.* **2016,** *2*, A41.
29. Klinger, M., More features, more tools, more CrysTBox. *J. Appl. Cryst.* **2017,** *50*, 1226-1234.
30. Altieri, A. S.; Hinton, D. P.; Byrd, R. A., Association of biomolecular systems via pulsed-field gradient NMR self-diffusion measurements. *J. Am. Chem. Soc.* **1995,** *117*, 7566-7567.
31. Stejskal, E. O.; Tanner, J. E., Spin diffusion measurements: Spin echoes in the presence of a time-dependent field gradient. *J. Chem. Phys.* **1965,** *42*, 288.
32. Millero, F. J.; Dexter, R.; Hoff, E., Density and viscosity of deuterium oxide solutions from 5-70 °C. *J. Chem. Eng. Data* **1971,** *16*, 85-87.
33. Klug, H. P.; Alexander, L. E., *X-ray diffraction procedures for polycrystalline and amorphous materials*. Wiley-Interscience: New York, 1974.
34. Semenyuk, A. V.; Svergun, D. I., GNOM– a program package for small-angle scattering data processing. *J. Appl. Crystallogr.* **1991,** *24*, 537-540.
35. Fissan, H.; Ristig, S.; Kaminski, H.; Asbach, C.; Epple, M., Comparison of different characterization methods for nanoparticle dispersions before and after aerosolization. *Anal. Meth.* **2014,** *6*, 7324-7334.
36. Guo, C.; Yarger, J. L., Characterizing gold nanoparticles by NMR spectroscopy. *Magn. Reson. Chem.* **2018,** *56*, 1074-1082.
37. Marbella, L. E.; Millstone, J. E., NMR techniques for noble metal nanoparticles. *Chem. Mater.* **2015,** *27*, 2721-2739.
38. Salassa, G.; Burgi, T., NMR spectroscopy: A potent tool for studying monolayer-protected metal nanoclusters. *Nanoscale Horiz.* **2018,** *3*, 457-463.
39. Chastain, J.; King Jr, R. C., Handbook of X-ray photoelectron spectroscopy. *Perkin-Elmer, USA* **1992**, 261.

40. Contour, J. P.; Mouvier, G.; Hoogewys, M.; Leclere, C., X-ray photoelectron spectroscopy and electron microscopy of Pt Rh gauzes used for catalytic oxidation of ammonia. *J. Catal.* **1977,** *48*, 217-228.
41. Nefedov, V. I.; Firsov, M. N.; Shaplygin, I. S., Electronic structures of MRhO2, MRh2O4, RhMO4 and Rh2MO6 on the basis of X-ray spectroscopy and ESCA data. *J. Electron Spectrosc. Rel. Phenom.* **1982,** *26*, 65-78.
42. Pitto-Barry, A.; Perdigao, L. M. A.; Walker, M.; Lawrence, J.; Costantini, G.; Sadler, P. J.; Barry, N. P. E., Synthesis and controlled growth of osmium nanoparticles by electron irradiation. *Dalton Trans.* **2015,** *44*, 20308-20311.
43. Pappert, K.; Loza, K.; Shviro, M.; Hagemann, U.; Heggen, M.; Dunin-Borkowski, R. E.; Schierholz, R.; Maeda, T.; Kaneko, K.; Epple, M., Nanoscopic porous iridium/iridium dioxide superstructures (15 nm): Synthesis and thermal conversion by in situ transmission electron microscopy. *Chem. Eur. J.* **2019,** *25*, 11048-11057.
44. Qiu, L.; Liu, F.; Zhao, L.; Yang, W.; Yao, J., Evidence of a unique electron donor−acceptor property for platinum nanoparticles as studied by XPS. *Langmuir* **2006,** *22*, 4480-4482.
45. Garcia, P. R. A. F.; Loza, K.; Daumann, S.; Grasmik, V.; Pappert, K.; Rostek, A.; Helmlinger, J.; Prymak, O.; Heggen, M.; Epple, M.; Oliveira, C. L. P., Combining small-angle x-ray scattering and x-ray powder diffraction to investigate size, shape and crystallinity of silver, gold and alloyed silver-gold nanoparticles. *Braz. J. Phys.* **2019,** *49*, 183-190.
46. Rostek, A.; Breisch, M.; Loza, K.; Garcia, P. R. A. F.; Oliveira, C. L. P.; Prymak, O.; Heggen, M.; Köller, M.; Sengstock, C.; Epple, M., Wet-chemical synthesis of Pd-Au core-shell nanoparticles (8 nm): From nanostructure to biological properties. *ChemistrySelect* **2018,** *3*, 4994-5001.
47. Prymak, O.; Jakobi, J.; Rehbock, C.; Epple, M.; Barcikowski, S., Crystallographic characterization of laser-generated, polymer-stabilized 4 nm silver-gold alloyed nanoparticles. *Mater. Chem. Phys.* **2018,** *207*, 442-450.
48. Hosseini, S.; Wetzel, O.; Kostka, K.; Heggen, M.; Loza, K.; Epple, M., Pathways for oral and rectal delivery of gold nanoparticles (1.7 nm) and gold nanoclusters into the colon: enteric-coated capsules and suppositories. *Molecules* **2021,** *26*, 5069.
49. Castner, D. G.; Hinds, K.; Grainger, D. W., X-ray photoelectron spectroscopy sulfur 2p study of organic thiol and disulfide binding interactions with gold surfaces. *Langmuir* **1996,** *12*, 5083-5086.
50. Muniz-Miranda, M.; Zoppi, A.; Muniz-Miranda, F.; Calisi, N., Palladium oxide nanoparticles: Preparation, characterization and catalytic activity evaluation. *Coatings* **2020,** *10*, 207.
51. Nichols, F.; Lu, J. E.; Mercado, R.; Dudschus, R.; Bridges, F.; Chen, S., Platinum oxide nanoparticles for electrochemical hydrogen evolution: influence of platinum valence state. *Chem. Eur. J.* **2020,** *26*, 4136-4142.
52. He, B.; Ha, Y.; Liu, H.; Wang, K.; Liew, K. Y., Size control synthesis of polymer-stabilized water-soluble platinum oxide nanoparticles. *J. Coll. Interface Sci.* **2007,** *308*, 105-111.
53. Reetz, M. T.; Koch, M. G., Water-soluble colloidal Adams catalyst: preparation and use in catalysis. *J. Am. Chem. Soc.* **1999,** *121*, 7933-7934.
54. Gao, M. R.; Lin, Z. Y.; Jiang, J.; Cui, C. H.; Zheng, Y. R.; Yu, S. H., Completely green synthesis of colloid adams' catalyst a-PtO2 nanocrystals and derivative Pt nanocrystals with high activity and stability for oxygen reduction. *Chem. Eur. J.* **2012,** *18*, 8423-8429.

55. Kim, Y. T.; Tadai, K.; Mitani, T., Highly dispersed ruthenium oxide nanoparticles on carboxylated carbon nanotubes for supercapacitor electrode materials. *J. Mater. Chem.* **2005,** *15*, 4914-4921.
56. Wang, W.; Guo, S.; Lee, I.; Ahmed, K.; Zhong, J.; Favors, Z.; Zaera, F.; Ozkan, M.; Ozkan, C. S., Hydrous ruthenium oxide nanoparticles anchored to graphene and carbon nanotube hybrid foam for supercapacitors. *Sci. Rep.* **2014,** *4*, 4452.
57. Zhao, Y.; Hernandez-Pagan, E. A.; Vargas-Barbosa, N. M.; Dysart, J. L.; Mallouk, T. E., A high yield synthesis of ligand-free iridium oxide nanoparticles with high electrocatalytic activity. *J. Phys. Chem. Lett.* **2011,** *2*, 402-406.
58. Thomas, J. M.; Thomas, W. J., *Principles and practice of heterogeneous catalysis*. VCH: Weinheim, 1996; p 670.
59. Rossi, L. M.; Fiorio, J. L.; Garcia, M. A. S.; Ferraz, C. P., The role and fate of capping ligands in colloidally prepared metal nanoparticle catalysts. *Dalton Trans.* **2018,** *47*, 5889-5915.

TOC graphics

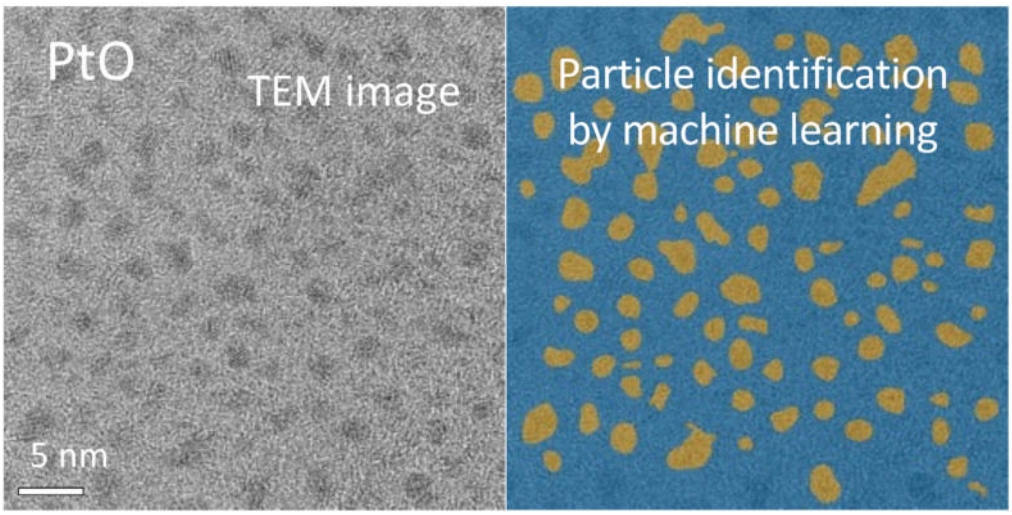

Synopsis

Hydrolysis and colloidal stabilization by glutathione yields ultrasmall nanoparticles of platinum group metal oxides (all six elements) with a typical core diameter of 1.8 nm. Their chemical nature was confirmed by X-ray photoelectron spectroscopy and X-ray powder diffraction, whereas a full chemical characterization was possible by elemental analysis, combined with quantitative NMR spectroscopy. Particles were identified in TEM images by machine learning.